# The effect of temperature and humidity fluctuations on the liquid water path of non-precipitating closed-cell stratocumulus clouds

Stephan R. de Roode[a,b]* and Alexander Los[a]

[a] *Royal Netherlands Meteorological Institute (KNMI), de Bilt, The Netherlands*
[b] *Dept. of Multi-Scale Physics, Delft University of Technology, Delft, The Netherlands*

**ABSTRACT:** The spatial variability of the liquid water path (LWP) is analyzed from a large-eddy simulation of the diurnal cycle of stratocumulus clouds as observed during FIRE I. In stratocumulus clouds, the temperature and the total specific humidity cannot fluctuate independently, but are tightly connected to fluctuations in the liquid water potential temperature. If the latter are relatively small, a strong positive correlation between the temperature and the total specific humidity can be expected. The effect of temperature fluctuations on the magnitude of liquid water fluctuations must be considered to properly compute the LWP distribution in stratocumulus clouds.

The simulated stratocumulus cloud fields are used to compute the albedo inhomogeneity factor $\chi$ according to the effective thickness approach. During the day, the mean LWP decreases due to short-wave radiative warming. Also, the probability density function for the LWP becomes positively skewed due to cumuli that have their base well below the mean stratocumulus cloud-base height. For this situation, the inhomogeneity factor $\chi$ displays a minimum value of about 0.85. For solid (unbroken) cloud with an assumed Gaussian distribution for the optical depth, we find that the minimum inhomogeneity factor will be about 0.8. This minimum value for the inhomogeneity factor, and that from the LES results, are larger than reported from FIRE I observations. Copyright © 2008 Royal Meteorological Society

## 1. Introduction

A cloud layer which exhibits horizontal variations in the liquid water path (LWP) will typically have a lower cloud albedo than a plane-parallel cloud that has exactly the same volume mean cloud LWP and microphysical structure (Harshvardhan and Randall, 1985). This plane-parallel albedo bias arises because the albedo of a cloudy column is a convex function of the cloud optical depth.

Large-scale models that do not have information on the subgrid variability of the LWP should therefore correct for the inhomogeneity factor as plane-parallel clouds will invariably have larger cloud albedos. Cahalan *et al.* (1994) analysed time series of marine stratocumulus LWPs observed off the coast of California during FIRE I (First International Satellite Cloud Climatology Project Regional Experiment, June 29–July 20, 1987). They showed that the observed albedos can be reproduced with the plane-parallel calculation if an effective cloud optical depth $\tau_{\text{eff}}$ is used, according to $\tau_{\text{eff}} = \chi\tau$. During FIRE, the inhomogeneity factor was estimated as $\chi = 0.7$ (Cahalan *et al.*, 1994). The use of this reduction factor, which is also referred to as the effective thickness

approximation (ETA), was implemented in the ECMWF model by Tiedtke (1996). However, Pincus *et al.* (1999) studied ship observations and satellite imagery of stratocumulus in the same region and found a much smaller albedo bias effect. The use of a constant reduction factor is questionable as its precise value depends on the mean and the variance of the cloud optical depth, which are controlled by the boundary-layer turbulence and the large-scale atmospheric circulation (Barker *et al.*, 1996; Los and Duynkerke, 2001; Rossow *et al.*, 2002; Bäuml *et al.*, 2004).

The McICA (Monte Carlo Independent Column Approximation) method is a fundamentally different approach to incorporate the effect of cloud horizontal inhomogeneity on radiation (Barker *et al.*, 2002; Pincus *et al.*, 2003; Barker and Räisänen, 2004; Räisänen *et al.*, 2004). This method is based on the generation of a cloud field on a column-by-column basis, while conserving the same value for the mean column LWP. The cloud generator uses information about layer cloud fraction, vertical overlap of cloud fraction and cloud condensate for adjacent layers, and density functions describing horizontal variations in cloud water content. The ICA assumes that the radiative transfer can be computed for every single subcolumn, which eliminates the need to correct for the albedo bias effect. The accuracy of the McICA procedure critically depends on a precise estimation of the subgrid

* Correspondence to: Stephan R. de Roode, Dept. of Multi-Scale Physics, Delft University of Technology, P.O. Box 5046, 2600 GA, Delft, The Netherlands.
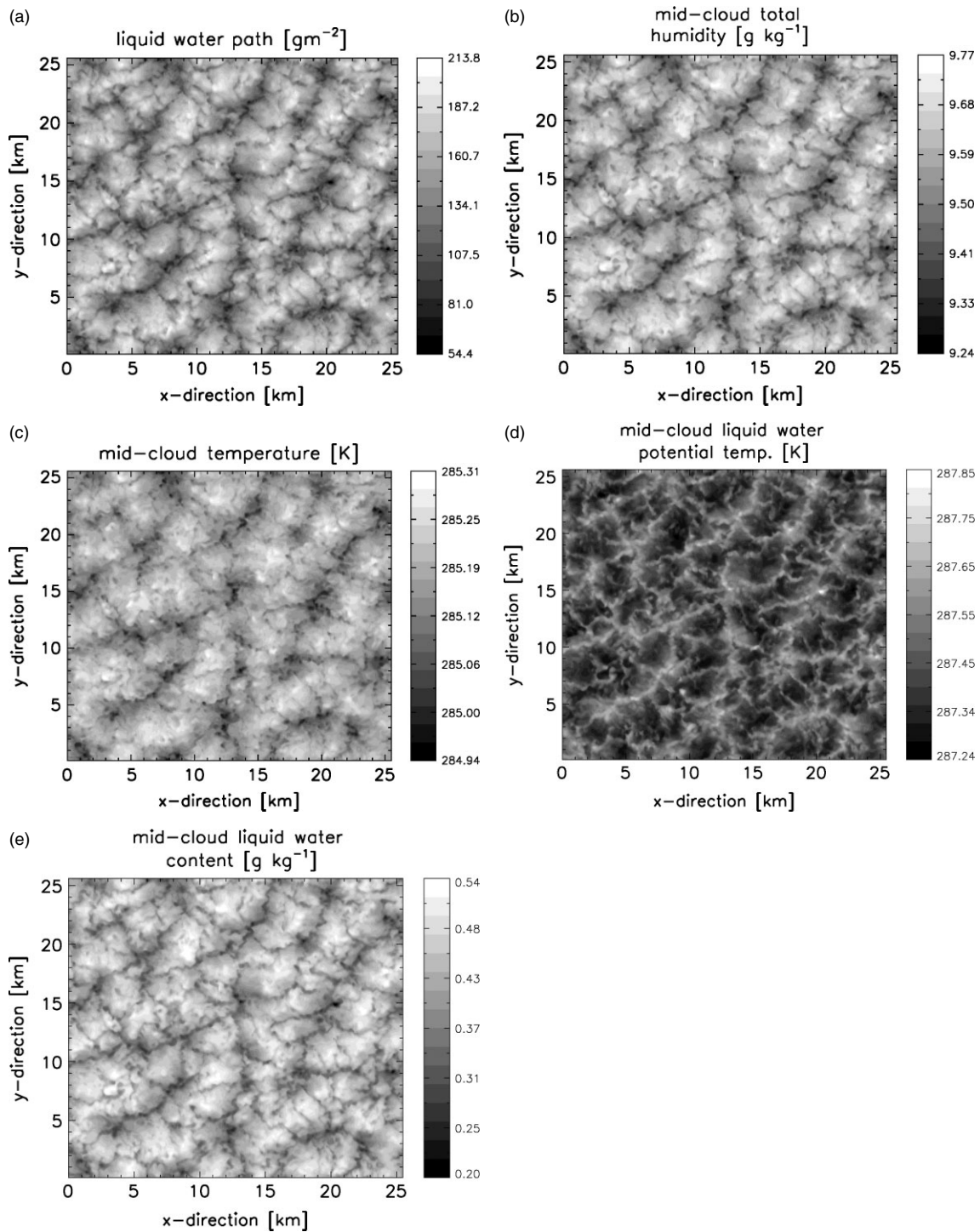E-mail: S.R.deRoode@tudelft.nl

Figure 1. Grey-scale plots of the instantaneous liquid water path, the total water specific humidity, the temperature, the liquid water content and the liquid water potential temperature fields in the middle of a stratocumulus cloud layer after 8 hours of simulation time on a large horizontal domain ($25.6 \times 25.6$ km$^2$). The fields were obtained from a large-eddy simulation of the diurnal cycle of stratocumulus off the coast of California as observed during FIRE I. The results show that the large-scale structures are nearly identical.

variability of the LWP and the cloud fraction.

In this study we analyse the effect of humidity and temperature fluctuations on the cloud liquid water variability. We analyse results from a large-eddy simulation (LES) of the the diurnal cycle of FIRE I stratocumulus. This case was set up as a model intercomparison case within the framework of the EUROCS (European Cloud Systems) project (Duynkerke *et al.*, 2004). To allow the

formation of mesoscale fluctuations by boundary-layer turbulence, the simulation was performed on a large horizontal domain of $25.6 \times 25.6$ km$^2$ (De Roode *et al.*, 2004). The motivation of this research can perhaps be best illustrated from the LES results displayed in Figure 1. It is clear that the modelled LWP, the in-cloud total water specific humidity, the temperature and the

liquid water content exhibit nearly identical spatial structures. Section 2 discusses in more detail some statistics of the LES results and compares them to observations reported by Wood and Taylor (2001). The effect of temperature fluctuations on liquid water fluctuations is discussed in sections 3 and 4. The diurnal variation of the inhomogeneity factor $\chi$ is computed from simulated FIRE I stratocumulus fields and is presented in section 5. Section 6 summarizes and discusses the major findings.

## 2. Large-eddy simulation of the diurnal cycle of stratocumulus as observed during FIRE I

### 2.1. Experimental set-up

The diurnal cycle of the FIRE I stratocumulus case is investigated from results obtained with the Dutch atmospheric LES (DALES) model. A large horizontal domain ($25.6 \times 25.6 \times 1.2$ km$^3$) was used with a horizontal (vertical) grid space of 100 (20) m. The model solves prognostic equations for the liquid water potential temperature $\theta_l = \theta - L_{vap}/(c_p \Pi)q_l$, the total water content $q_t = q_{vap} + q_l$ and the $u$, $v$ and $w$ components of the wind velocities. Here $\Pi = T/\theta$ indicates the Exner function, $q_{vap}$ ($q_l$) is the (liquid water) specific humidity, $\theta$ is the potential temperature, $L_{vap}$ is the latent heat of vaporization, $c_p$ is the isobaric specific heat for dry air, and $\epsilon_I = 1/\epsilon - 1 \approx 0.608$, where $\epsilon = R_d/R_{vap}$, the ratio of the specific gas constants for dry air and water vapour. Note that in the absence of cloud liquid water, $\theta_l = \theta$. The LES model does not take into account drizzle, in which case the quantities $\theta_l$ and $q_t$ are conserved for adiabatic processes that involve condensation or evaporation. The simulated stratocumulus cloud layer studied here can therefore be best regarded as a polluted cloud, which is less likely to produce precipitation than stratocumulus in a very clear environment. The grid-box mean of the liquid water content is diagnosed from the grid-box mean values of $\theta_l$ and $q_t$. We use overbars to indicate the slab average over the horizontal domain of the model, and primes to denote the deviation from the horizontal slab mean, e.g. $\overline{\theta_l}$ and $\theta_l'$.

The initial (thermo)dynamic state was based on radiosonde observations of temperature and relative humidity vertical profiles collected during the FIRE I stratocumulus experiment (Duynkerke *et al.*, 2004). The effects of large-scale horizontal advection and radiative flux divergence in the free atmosphere were accounted for by prescribed fixed, height-dependent tendencies. In addition, the large-scale subsidence rate was prescribed.

### 2.2. Simulated evolution of the cloud layer

The simulated evolution of the stratocumulus cloud boundaries are displayed in Figure 2. The cloud top is capped by a very strong inversion. The gradual increase of the cloud-top height during the night and a lowering during the day reflect a competition between the large-scale subsidence and the entrainment rate. The boundary-layer height is in a steady state if the entrainment rate balances the large-scale subsidence. The latter tends to advect the boundary-layer height downwards, whereas turbulent mixing of free atmosphere air into the boundary layer acts to counteract this process. During the day, absorption of solar radiation warms the cloud layer which causes a weak stable stratification near the base of the cloud. As a result, the turbulence intensity in the cloud layer weakens and the entrainment rate decreases.

Because the cloud top is capped by a stable inversion layer, the standard error of the cloud-top height is quite small, indicating a rather homogeneous spatial distribution of cloud-top heights. On the contrary, the mean cloud-base height shows much larger fluctuations with time. However, note that after about 10 hours simulation time, thermals that are triggered from the surface reach saturation at almost a constant height, as can be seen from a nearly constant lowest cloud-base height.

The mean cloud LWP is defined by

$$\overline{LWP} = \rho_0 \int_0^{z_{top}} \overline{q_l}(z) \, \mathrm{d}z, \tag{1}$$

with $\rho_0$ the mean air density (which is necessary if $q_l$ has units kg kg$^{-1}$ rather than kg m$^{-3}$), and $z_{top}$ the top of the LES domain. The mean LWP has a maximum during the night and a minimum during the day. Note the relatively large maximum LWPs in the LES domain during the simulation time, which can be explained from cloud columns that have a relatively low cloud base and a top close to the mean inversion layer height. Thumbnail plots of the simulated LWP probability density functions (PDFs) are displayed in Figure 3.

Figure 4 shows the temporal evolution of the skewness for the LWP,

$$S_{LWP} = \frac{\overline{LWP'^3}}{\overline{LWP'^2}^{3/2}}, \tag{2}$$

and likewise for the skewness of the total specific humidity, $S_{q_t}$, in the middle of the cloud layer at 450 m. During the first night (00–08 local time) $S_{LWP}$ is negative, but during the second night its near-zero values indicate that the PDF of the LWP is more or less symmetric. The positive values for $S_{LWP}$ during daytime are due to thermals that become saturated well below the mean cloud-base height. Positive values $S_{LWP}$ are accompanied by positive values for $S_{q_t}$ in the middle of the cloud layer. These results are similar to FIRE I observations analyzed by Wood and Taylor (2001). They showed that for the case where the mean LWP is small and the cloud-base height distribution is fairly broad, the observations exhibit a positively skewed distribution for the LWP.

### 2.3. Spectral properties

Figure 5 shows energy density spectra of the LWP at four different times. These spectra were obtained from a Fourier transformation, which provides a two-dimensional matrix of the (co-)spectral energy, $E(k_x, k_y)$.
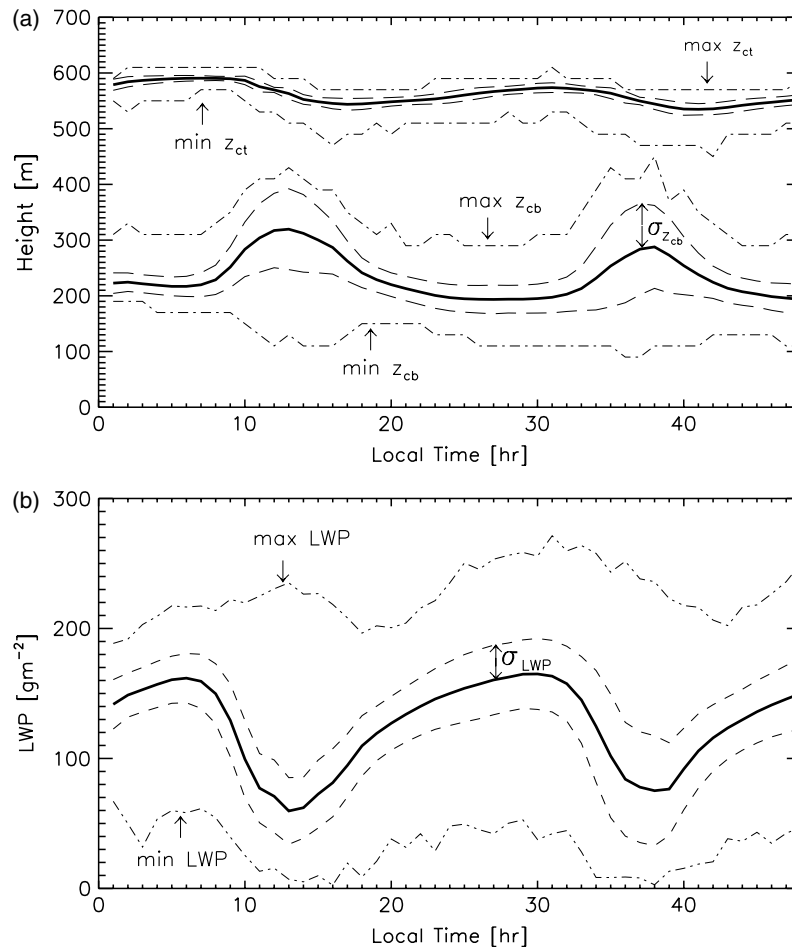
Figure 2. The simulated diurnal cycle of (a) the cloud-top and cloud-base heights and (b) the liquid water path. The results were obtained from hourly instantaneous simulated stratocumulus cloud fields. The bold solid lines indicate the mean values, the dashed lines show one standard deviation from the mean, and the dash-dot lines show the minimum and maximum values in the LES domain.

The spectral energy density ($E/\mathrm{d}k$), with $\mathrm{d}k$ the wavenumber interval. The energy density spectra shown in the figure are plotted as a function of the wavenumber $k = (k_x^2 + k_y^2)^{1/2}$. The minimum wavenumber $k_{\min} = 1/25600$ m$^{-1}$ is determined by the horizontal domain size of the LES model. From the start of the simulation, the LWP variance at the largest length-scales gradually grows with time. After 36 hours simulation time, the LWP spectral energy is a maximum at the smallest wavenumber. Wood and Hartmann (2006) found from MODIS data of marine low cloud over the eastern subtropical oceans that the LWP spatial variance is dominated by horizontal scales of 10–50 km, where larger length-scales are indicative for mesoscale cellular convection. Note that in a LES the growth of fluctuations at the mesoscales is due to turbulence convection only (Jonker et al., 1999; De Roode et al., 2004).

Energy density spectra for $T$, $q_t$ and $\theta_v$ in the middle of the subcloud layer and the middle of cloud layer at $t = 36$ local time are shown in Figure 6. Figure 6(c) shows that the temperature and total specific humidity exhibit a strong positive correlation in the cloud layer. Observations collected in the subcloud layer of various stratocumulus cases analyzed by Wood and Taylor (2001)

show negative correlations at scales larger than the boundary-layer depth. The LES fields in the subcloud layer also indicate negative correlations between the total specific humidity and temperature at all length-scales (Figure 6(c)). This result can be qualitatively understood from the vertical flux profiles (not shown here). In the simulations, the buoyancy flux tends to become negative above the middle of the subcloud layer up to the cloud-base height, whereas the total specific humidity flux is positive from the surface to the cloud top. These flux profiles are quite common in stratocumulus cloud layers (Nicholls, 1984). In clear unsaturated air, fluctuations of the virtual potential temperature are, to a good approximation, given by

$$\theta_v' = T' + 0.61\overline{\theta_v}q_{vap}'. \qquad (3)$$

Therefore, for parcels with $\theta_v' < 0$ and $q_{vap}' > 0$, this means that $T' < 0$ in order to satisfy (3). Note that in the subcloud layer the spectral variance of the temperature is slightly larger than that of the virtual potential temperature. From the expression above we can derive

$$\theta_v'^2 = T'^2 + (0.61\overline{\theta_v})^2 q_{vap}'^2 + 2 \cdot 0.61\overline{\theta_v}T'q_{vap}', \qquad (4)$$
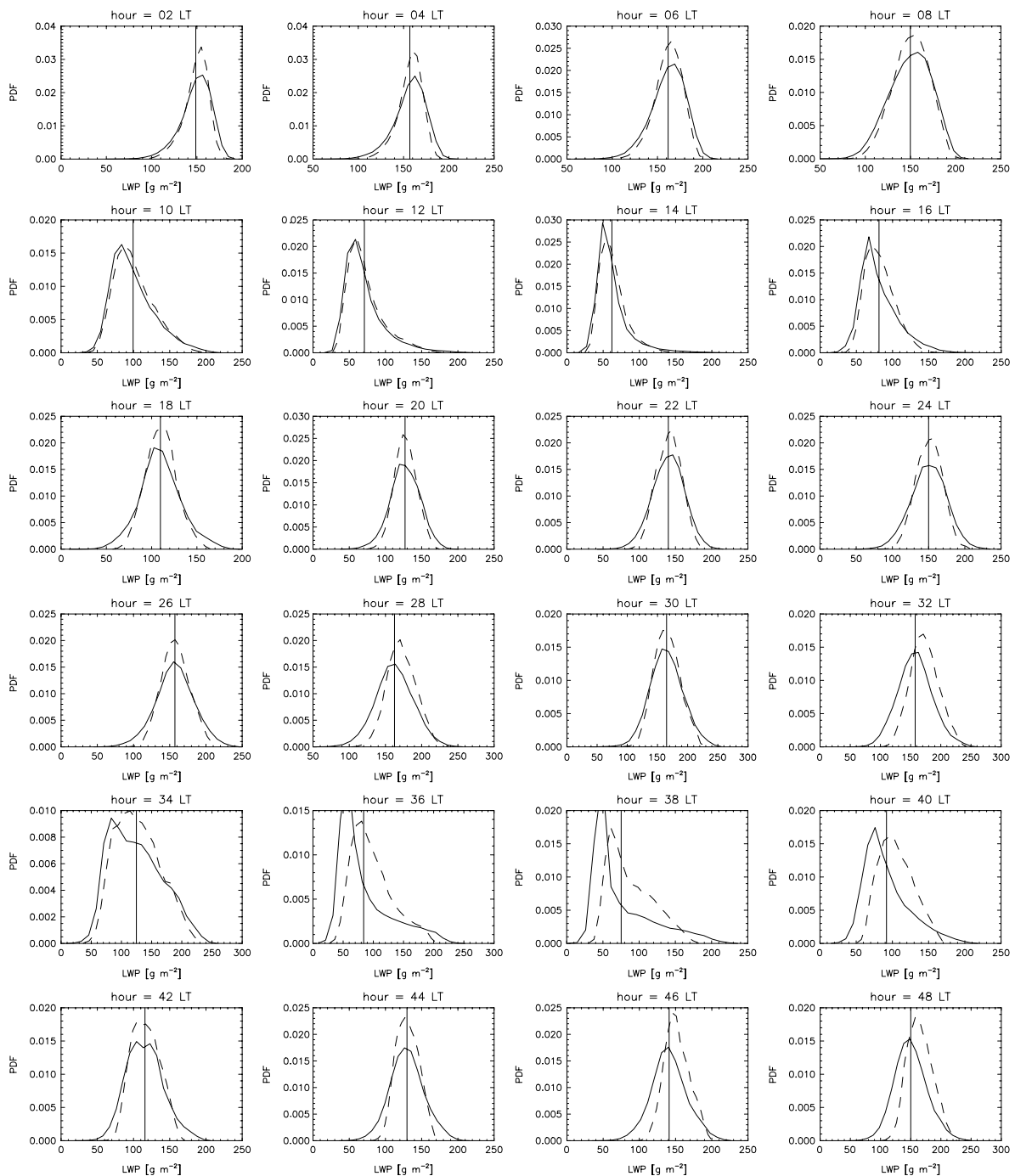
Figure 3. Thumbnail time series of LWP probability density functions at 2-hour intervals. The solid lines indicate PDFs which were computed directly from the 3D LES liquid water content fields, and the dashed lines represent reconstructed PDFs based on the total specific humidity fields in the middle of the cloud layer at 450 m according to Equation (26). The vertical solid lines indicate the mean LWPs.

from which it directly follows that the temperature and the specific humidity must be negatively correlated if the sum of their respective (spectral) variances is larger than the variance of $\theta_v$.

## 3. Temperature and humidity correlations in the stratocumulus cloud layer

### 3.1. LES results

Figure 7 shows that the LWP and $q_t$ in the middle of the cloud layer (at 450 m) are well correlated. Relatively

large $q_t$ values correspond to larger LWPs, and vice versa. During the day, the slightly curved shape in the scatter plot of $q_t$ and LWP fluctuations is due to a more inhomogeneous cloud structure with cumulus clouds penetrating a relatively thin stratocumulus layer above.

Figure 8 shows scatter plots of $T'$ and $q_t'$ in the middle of the cloud layer. Relatively moist air parcels appear to be relatively warm, and vice versa. In particular, during night-time $T'$ and $q_t'$ satisfy an approximate linear relationship
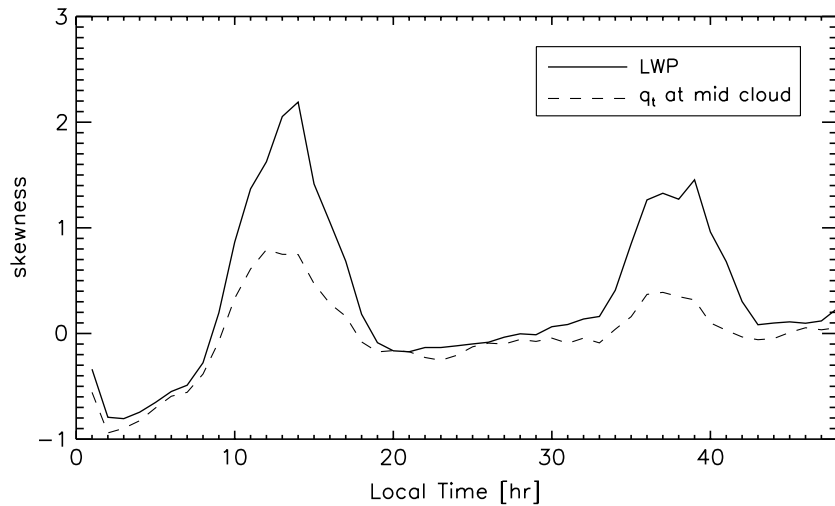
$$T' = c_{qT} q_t', \qquad (5)$$

Figure 4. The skewness of the cloud liquid water path (solid line) and total specific humidity in the middle of the cloud layer (dashed line) as a function of time.
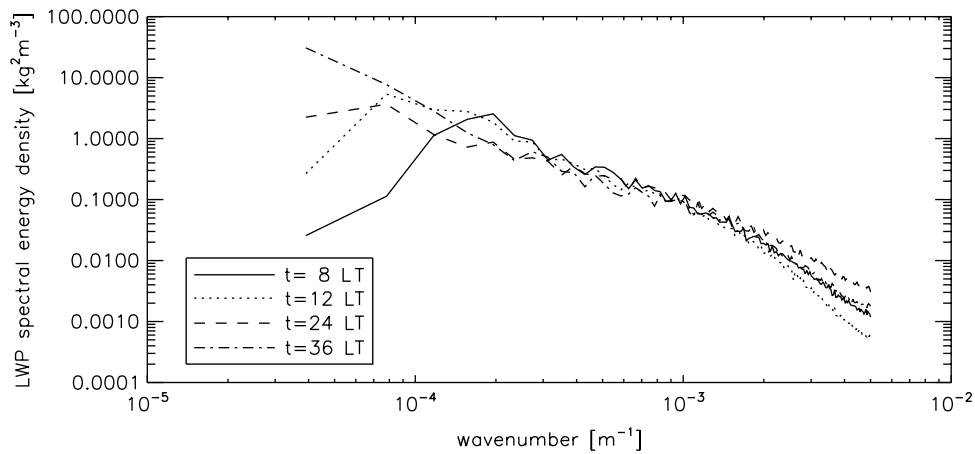


Figure 5. Energy density spectra of the liquid water path. The results were obtained from the LES fields at $t = 8$, 12, 24 and 36 hours local time.

where the factor $c_{qT}$ represents the slope of the linear fit shown in the figure.

To calculate $q_l'$ fluctuations from $q_t'$ fluctuations, one needs to account for fluctuations of the saturation specific humidity $q_{sat}'$ according to

$$q_l' = q_t' - q_{vap}' = q_t' - q_{sat}'(T). \qquad (6)$$

Fluctuations in the saturation specific humidity $q_{sat}$ can be calculated from temperature fluctuations according to the Clausius – Clapeyron relation (Nicholls, 1984).

$$q_{sat}' = \left(\frac{dq_{sat}}{dT}\right) T' = \gamma T', \qquad (7)$$

with $\gamma \equiv dq_{sat}/dT$. In the middle of the cloud layer, the mean temperature is about $12\,°C$ and $\gamma \approx 0.6$ g kg$^{-1}$ K$^{-1}$. Using (7), and substitution of (5) in (6) yields an expression for $q_l'$ which depends on $q_t'$ only:

$$q_l' = q_t' \left(1 - \gamma c_{qT}\right) \equiv \beta q_t', \qquad (8)$$

which defines the $\beta$ factor. Figure 9 shows that the PDF for $q_t$ is much broader than for $q_l$, which indicates that $\beta < 1$.

The fact that $q_t$ and $T$ are well correlated can be understood by considering the expression for the liquid water potential temperature fluctuations,

$$\theta_l' = \theta' - \frac{L_v}{c_p}q_l' = T'\left(1 + \frac{L_v}{c_p}\gamma\right) - \frac{L_v}{c_p}q_t', \qquad (9)$$

where we used (6), (7) and the approximation $T' \approx \theta'$. Temperature fluctuations can therefore be written as

$$T' = A_w\theta_l' + B_w q_t', \qquad (10)$$

which explains why in the cloud layer $T$ and $q_t$ cannot vary independently. The factor

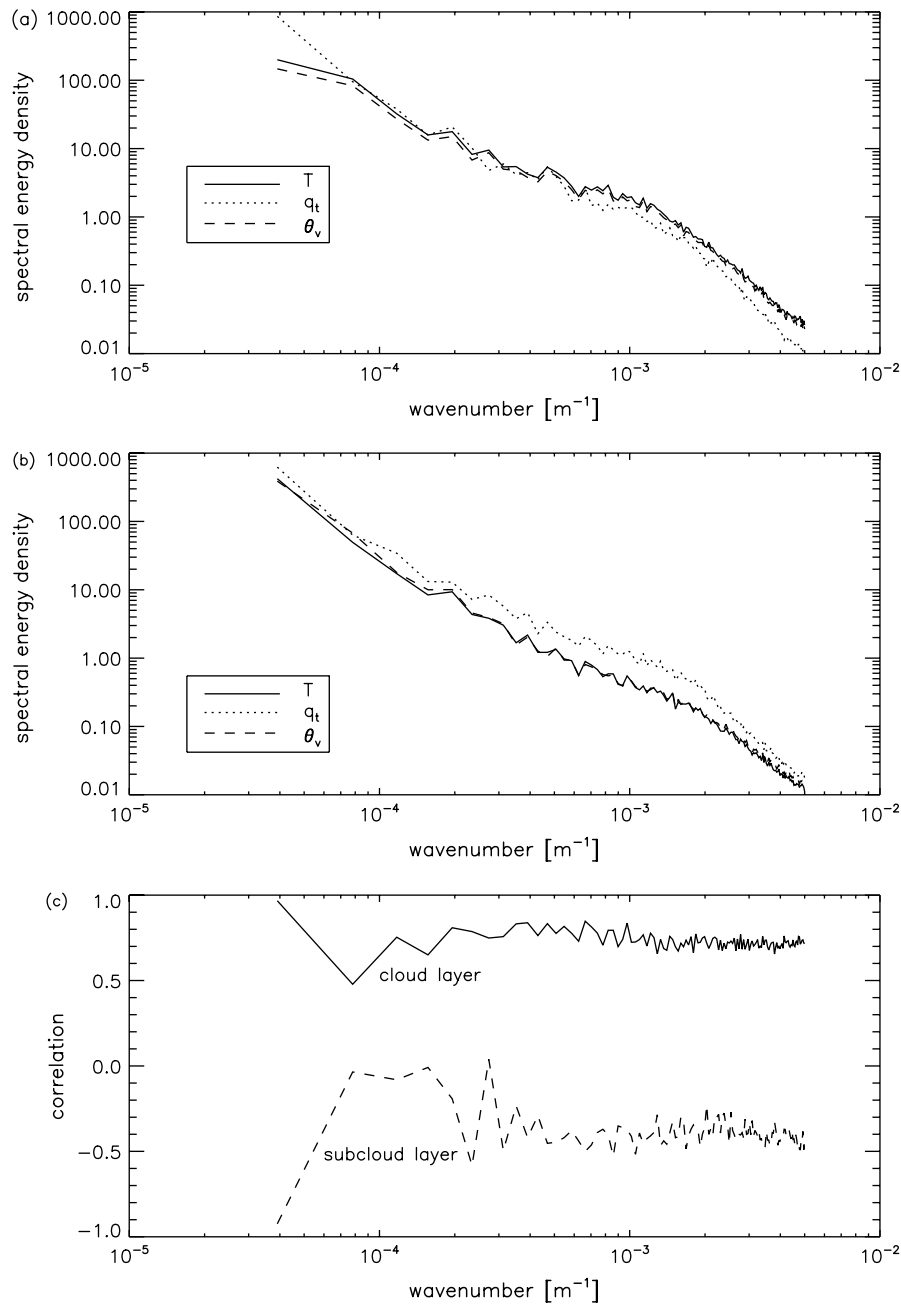$$A_w = \left(1 + \frac{L_{vap}}{c_p}\gamma\right)^{-1}$$

Figure 6. Energy density spectra of the temperature ($T$), total water specific humidity ($q_t$ in g kg$^{-1}$) and the virtual potential temperature ($\theta_v$) in (a) the middle of the subcloud layer at 210 m and (b) the middle of the cloud layer at 450 m. (c) shows the spectral correlation of the temperature and total specific humidity in the middle of the cloud and subcloud layers. The results were obtained from the LES fields at $t = 36$ hours local time.

depends weakly on the temperature and has a value of about 0.4 in the middle of the cloud layer, and

$$B_w = \frac{L_{vap}}{c_p}\left(1 + \frac{L_{vap}}{c_p}\gamma\right)^{-1} \approx 1000 \text{ K}.$$

Figure 10 shows that the variance $A_w^2\overline{\theta_l'^2}$ is much smaller than $\overline{T'^2}$. In that case, one may approximate

$$T' \approx B_w q_t'. \qquad (11)$$

The slope in the scatter plot of $q_t'$ and $T'$ for the night-time case displayed in Figure 8 is about equal to $B_w$.

In case $\theta_l$ fluctuations can be neglected, a comparison of (5) and (11) shows that the $\beta$ factor can be expressed as

$$\beta|_{\theta_l'=0} = (1 - \gamma B_w). \qquad (12)$$

In the middle of the cloud layer, $\beta|_{\theta_l'=0} \approx 0.4$. Thus, according to (12) the magnitude of $q_l$ fluctuations is more than halved if $\theta_l$ fluctuations are ignored rather than $T$ fluctuations. We have used the LES cloud fields to directly compute the $\beta$ factor as defined by (8). The factor $c_{qT}$ was obtained from a linear fit of the total specific humidity and temperature in the middle of the
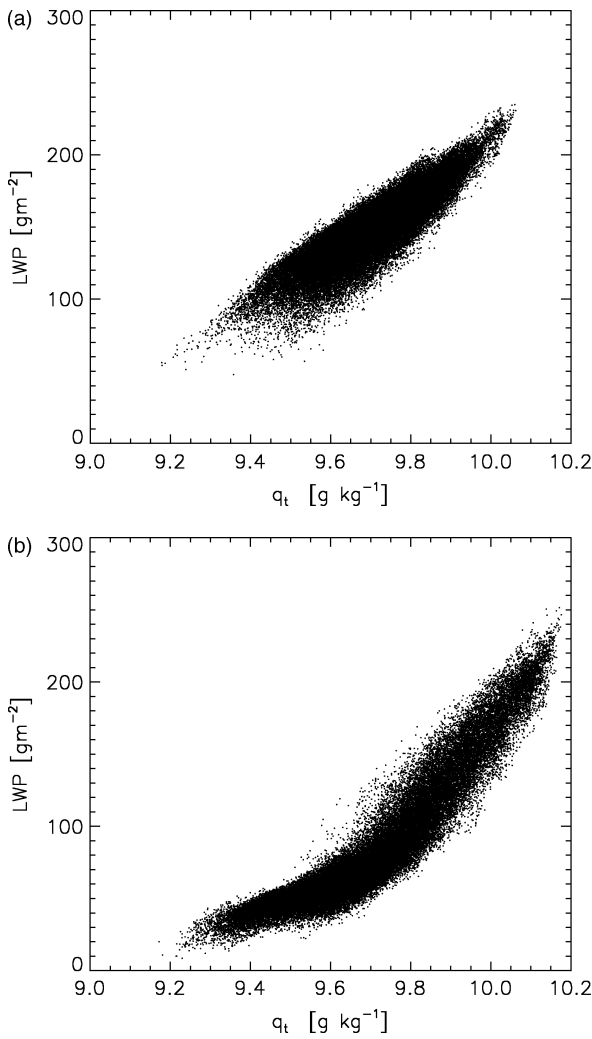
Figure 7. Scatter plots of the total specific humidity, $q_t$, in the middle of the cloud layer and the liquid water path during (a) the night at $t = 24$ hours local time and (b) the daytime at $t = 36$ hours local time.



Figure 8. Scatter plots of total specific humidity, $q_t'$, and temperature, $T'$, fluctuations in the middle of the cloud layer during (a) the night at $t = 24$ hours local time and (b) the daytime at $t = 36$ hours local time. The straight lines indicate the linear regression fit.

cloud layer. Figure 11 shows a weak diurnal variation of the $\beta$ factor. Overall, the $\beta$ factor has values rather close to 0.4. This means that for the FIRE I case the effect of temperature fluctuations on liquid water fluctuations should not be neglected.

### 3.2.   Analysis of flux profiles

Vertical turbulent fluxes of $\theta_l$ and $q_t$ at the stratocumulus cloud top can be diagnosed straightforwardly from the so-called flux-jump relation (Lilly, 1968),

$$\overline{w'\psi'}_T = -w_e \times \Delta\overline{\psi}, \qquad (13)$$

with $\Delta\overline{\psi}$ the mean jump of $\psi \in \{q_t, \theta_l\}$ across the inversion, and $w_e$ the entrainment rate. The entrainment rate (m s$^{-1}$) is the rate with which turbulent eddies mix air from just above the inversion air into the boundary layer.

If the air above the stratocumulus layer is clear, then the top of the stratocumulus cloud is cooled because more long-wave radiation is emitted than is absorbed
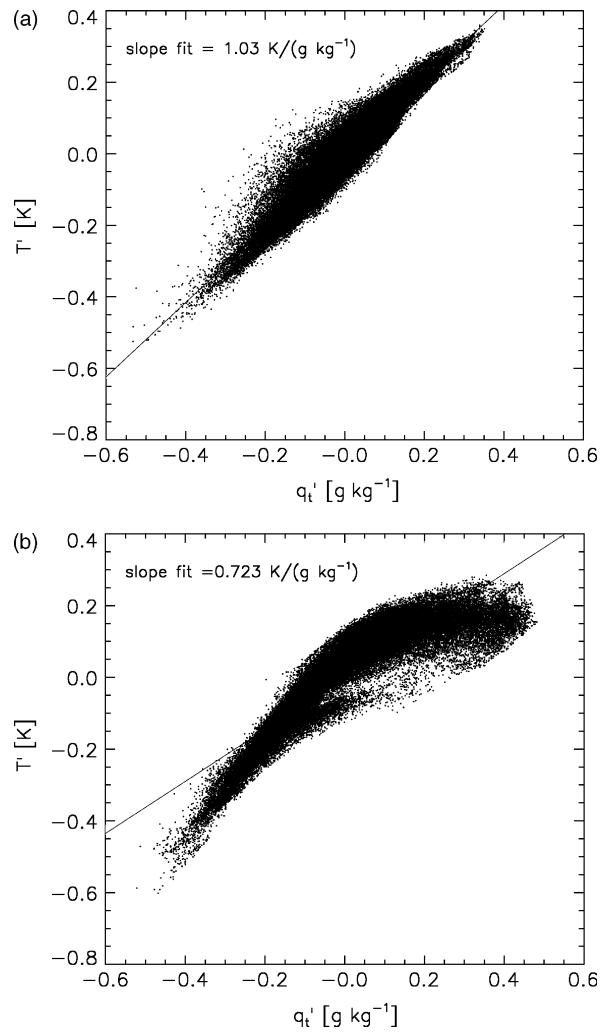
from above. The vertical divergence of the net long-wave radiative flux near the top of the cloud layer is typically about $\Delta F_L \approx 70$ W m$^{-2}$, and occurs in a layer of only a few tenths of metres thick. Just below the layer which is radiatively cooled (we will indicate fluxes at this level by a primed subscript $_{T'}$) the vertical turbulent flux of $\theta_l$ can then be expressed as (Nicholls, 1984; Stevens, 2002)

$$\overline{w'\theta_l'}_{T'} = -w_e\Delta\overline{\theta}_l + \frac{\Delta F_L}{\rho_0 c_p}. \qquad (14)$$

This formula is valid for a boundary layer that is in a quasi-steady state, meaning that the temporal change of the mean of $\theta_l$ and $q_t$ is constant with height. Furthermore we assume that the depth of the radiatively cooled layer is sufficiently small in order to approximate the total humidity flux $\overline{w'q_t'}_{T'}$ by the flux-jump formula (13).

Using (10), we can express the temperature flux in the cloud layer as

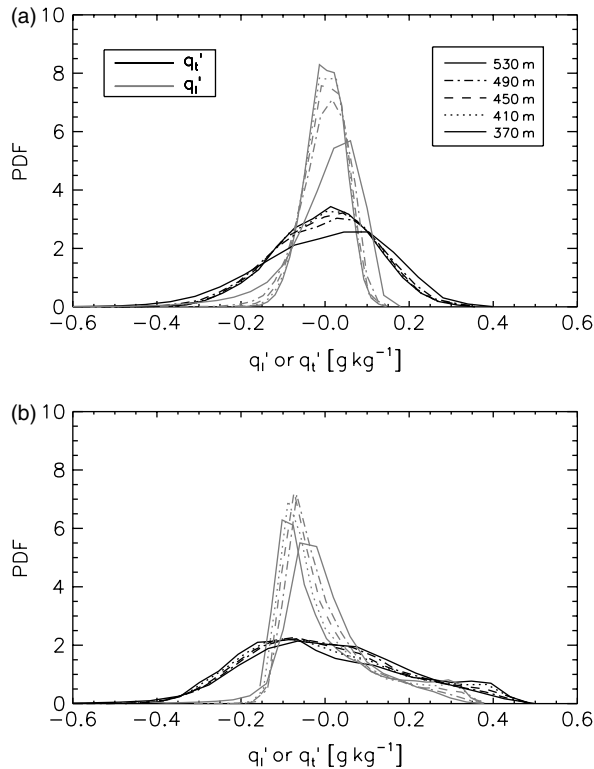$$\overline{w'T'} = A_w\overline{w'\theta_l'} + B_w\overline{w'q_t'}. \qquad (15)$$

Figure 9. Probability density functions for the total water specific humidity ($q'_t$, black lines) and the liquid water content ($q'_l$, grey lines) at five different heights in the cloud layer. (a) shows the results during the night at $t = 24$ hours local time and (b) during the day at $t = 36$ hours local time. Line styles are shown in (a).
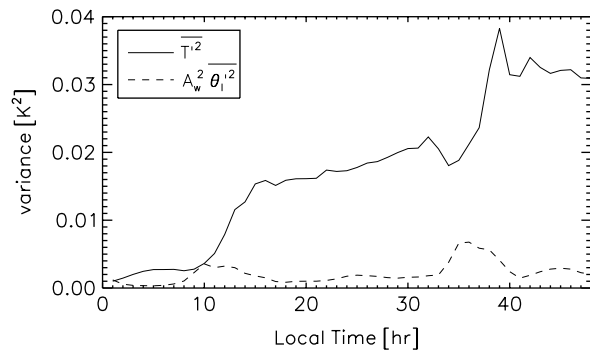


Figure 10. The liquid water potential temperature variance $\overline{\theta'^2_l}$ multiplied by a factor $A^2_w$, and the temperature variance $\overline{T'^2}$ in the middle of the cloud layer as a function of local time.

To explore which of the two fluxes on the right-hand side of (15) dominates the temperature flux, we define the ratio $R$ as

$$R \equiv \frac{\overline{w'T'}}{B_w \overline{w'q'_t}} = \frac{A_w \overline{w'\theta'_l}}{B_w \overline{w'q'_t}} + 1. \qquad (16)$$

The quantity $R$ is unity if the contribution of the liquid water potential temperature flux to the temperature flux is zero. If we use an entrainment parametrization, the value of $R$ near the cloud top can be computed.

Moeng (2000) presents an entrainment parametrization for stratocumulus clouds

$$w_e = \frac{1}{\Delta\theta_l} \left[ 0.2\overline{w'\theta'}_0 + \frac{\Delta F_L}{\rho_0 c_p} \right.$$
$$\left. \times \left\{ 2.5 - 2\exp(-\sqrt{b_m LWP}) \right\} \right], \qquad (17)$$

with $b_m = 0.9$ m² kg⁻¹. Note that Moeng's parametrization depends only on $\Delta\theta_l$, the potential temperature flux at the surface $\overline{w'\theta'}_0$, and $\Delta F_L$, whereas other entrainment parametrizations reviewed by Stevens (2002) do also depend on $\Delta q_t$ and the humidity flux at the surface $\overline{w'q'_{t0}}$. Substitution of (17) in (14) yields

$$\overline{w'\theta'_l}_{T'} = -0.2\overline{w'\theta'}_0 - \frac{\Delta F_L}{\rho_0 c_p}$$
$$\times \left\{ 1.5 - 2\exp(-\sqrt{b_m LWP}) \right\}. \qquad (18)$$

Using the entrainment rate parametrization (17) and the flux-jump relation (13), $R$ can be computed as a function of the inversion jumps $\Delta\theta_l$ and $\Delta q_t$. We used $\overline{w'\theta'}_0 = 0.01$ K m s⁻¹, $\Delta F_L = 70$ W m⁻², and $LWP = 0.150$ kg m⁻² to calculate the results presented in Figure 12. The inversion jumps of the FIRE I stratocumulus case are also depicted in the figure. In particular for humidity jumps $\Delta q_t < -2$ g kg⁻¹, $R$ is positive and is rather close to unity. This implies that, near the top of the cloud layer, the temperature flux will be dominated by the total humidity flux. In that case the correlation between the temperature and the total specific humidity will likely be positive.

## 4. A simple model to predict LWP fluctuations from the total specific humidity

On the basis of the LES results, we develop a simple model to predict the PDF of LWP that uses an assumed distribution of total specific humidity fluctuations. In a large-scale model, the latter may be computed by parametrizing the prognostic equation for the total specific humidity variance (Tompkins, 2002).

First of all, we assume that the vertical profile of the liquid water content in any cloudy subcolumn in the LES domain is given by a 'pseudo-adiabatic' mean liquid water vertical gradient $\alpha$ that is based on the actual modelled $\overline{LWP}$. With the aid of (1), the slope $\alpha$ can be expressed as

$$\alpha = \frac{2\overline{LWP}}{\rho_0 \overline{H}^2} \qquad \Longleftrightarrow \qquad \overline{LWP} = \frac{1}{2}\rho_0 \alpha \overline{H}^2, \quad (19)$$

with $\overline{H} = \overline{z_{top}} - \overline{z_{base}}$ the mean cloud-layer depth. For a vertically well-mixed stratocumulus layer, $\alpha$ will be close to the moist adiabat. For a constant slope $\alpha$ the pseudo-adiabatic maximum mean liquid water is proportional to the mean cloud-depth height,

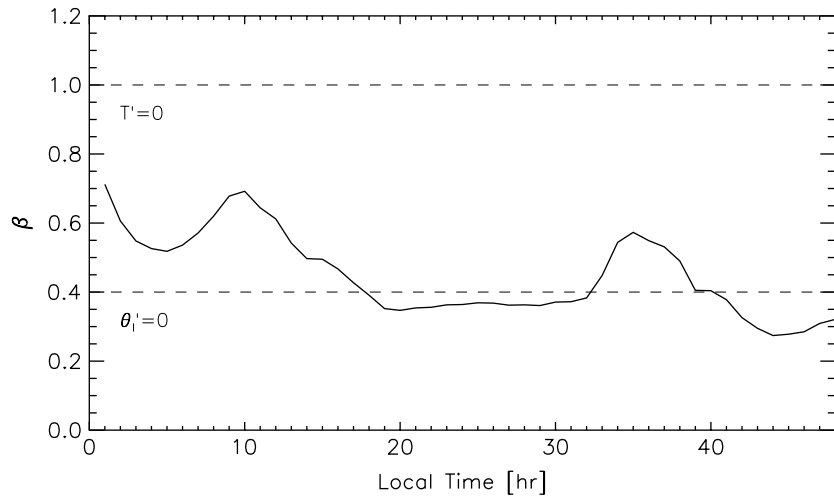$$\overline{q_{l\max}} = \alpha \overline{H}. \qquad (20)$$

Figure 11. Time series of the $\beta$ factor according to Equation (8) computed from the temperature and total specific humidity fields in the middle of the cloud layer. The two lines indicated by $T' = 0$ and $\theta'_l = 0$ correspond to the theoretical solutions for $\beta$ if either temperature or liquid water potential temperature fluctuations are neglected, respectively.
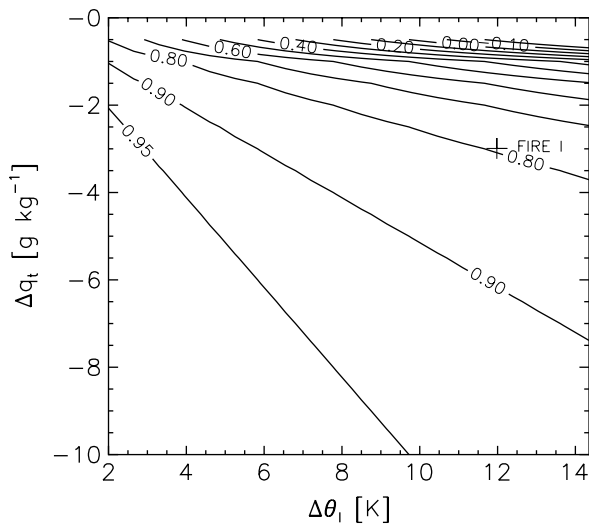


Figure 12. Contour plot of the parameter $R$ defined by Equation (16) as a function of the inversion jumps $\Delta\theta_l$ and $\Delta q_t$. The values for the FIRE I stratocumulus case are also shown.

As a next step, we have to predict the vertical variation of liquid water fluctuations in cloudy subcolumns. From the LES results we have computed the subcolumn vertical mean liquid water fluctuation according to

$$[q'_l](x, y) = \frac{\int_{z_{\text{base}}(x,y)}^{z_{\text{top}}(x,y)} \{q_l(x, y, z) - \overline{q_l}(z)\} \, dz}{z_{\text{top}}(x, y) - z_{\text{base}}(x, y)}. \quad (21)$$

Figure 13 shows that $[q'_l]$ correlates well with the subcolumn liquid water content fluctuation $q'_l$ in the middle of the mean cloud layer. We use this result to assume that the liquid water content fluctuation in a cloudy subcolumn can be approximated to be constant with height, except near the cloud base where the liquid water content increases linearly with height (see Figure 14 for a schematic).
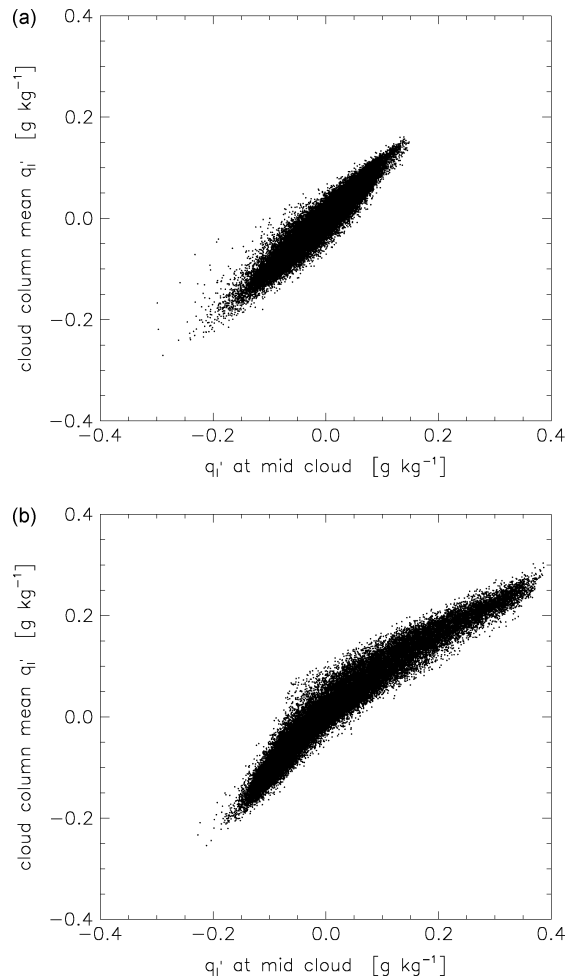


Figure 13. Scatter plots of liquid water content fluctuations $q'_l$ in the middle of the cloud layer and the subcolumn vertical cloud mean value $[q'_l]$ during (a) the night at $t = 24$ hours local time and (b) the daytime at $t = 36$ hours local time.

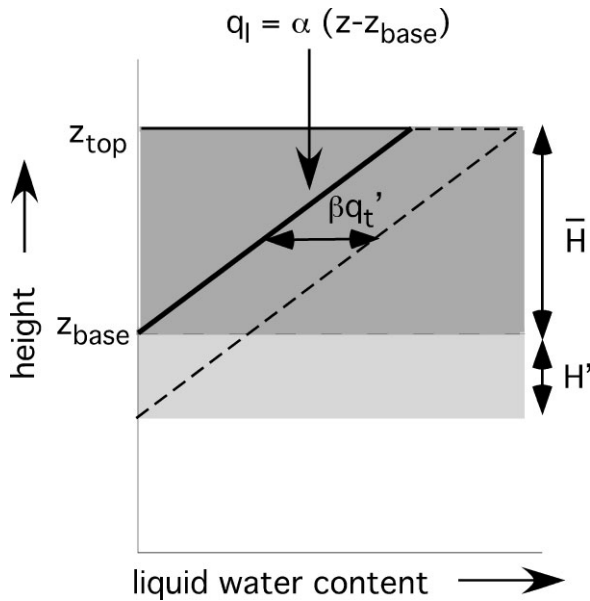Third, like Considine et al. (1997), Los and Duynkerke (2000) and Wood and Taylor (2001), we will assume

Figure 14. Schematic illustration of an assumed mean state for which the mean liquid water content $\overline{q_l}$ follows a pseudo-adiabatic vertical profile with slope $\alpha$. Given height-independent fluctuations of the liquid water content $q_l' = \beta q_t'$, subcolumn vertical liquid water profiles are computed by assuming that they are dictated by the same mean slope $\alpha$. All cloudy subcolumns are assumed to have the same mean cloud-top height. A vertical integration of the subcolumn liquid water vertical profile yields the subcolumn liquid water path.

that the stratocumulus cloud-top height variability is negligibly small. According to the LES results shown in Figure 2, this is a justifiable assumption for the FIRE I stratocumulus case. For an arbitrary cloudy subcolumn, the maximum liquid water content $q_{l,max}$ can then be written as

$$q_{l,max} = \overline{q_l}_{max} + q_l'. \tag{22}$$

Let us write the local cloud depth as $H = \overline{H} + H'$. Because the vertical gradient $\alpha$ applies to all cloudy subcolumns, $q_{l,max} = \alpha H$, and from (20) it follows that

$$H' = \frac{q_l'}{\alpha}. \tag{23}$$

Similar to (19), the local LWP can be expressed as

$$LWP = \frac{1}{2}\rho_0\alpha(\overline{H} + H')^2 = \frac{\rho_0}{2\alpha}(\alpha\overline{H} + q_l')^2. \tag{24}$$

After subtracting the mean LWP we obtain

$$LWP' = \rho_0\overline{H}q_l' + \frac{\rho_0 q_l'^2}{2\alpha}. \tag{25}$$

With the aid of (8), we can substitute out $q_l'$ fluctuations:

$$LWP' = \rho_0\overline{H}\beta q_t' + \frac{\rho_0\beta^2 q_t'^2}{2\alpha}. \tag{26}$$

The first term on the right-hand side of (26) gives $LWP' = \rho_0\overline{H}\beta q_t'$, which is proportional to the area of the parallelogram with height $\overline{H}$ and width $\beta q_t'$. Likewise,

with aid of (8) and (23), the second term can be rewritten as $LWP' = \rho_0 H'\beta q_t'/2$, which is proportional to the area of the triangle having a height $H'$ and base length $\beta q_t'$. If $\beta > 1$, then cloudy subcolumns are relatively moist and cold (or dry and warm), causing liquid water content fluctuations to be enhanced by a local lower (higher) temperature, and vice versa for $\beta < 1$.

Examples of actual and constructed PDFs for the LWP fluctuations are shown in Figure 3. The total specific humidity fluctuations $q_t'$ are taken from the LES results at a height of 450 m, which is at about the middle of the cloud layer. The $\beta$ factors were computed from linear fits of the temperature and total specific humidity, according to the results shown in Figure 11. The reconstructed PDFs for the LWP agree satisfactorily with the actual LWP distribution. If we neglect temperature fluctuations by using $\beta = 1$, then the reconstructed PDFs for the LWP become much too broad.

## 5. Albedo bias

The delta-Eddington radiative transfer equation (Joseph *et al.*, 1976) and the I3RC Monte Carlo model (Cahalan *et al.*, 2005) were used to compute the albedos from instantaneous, hourly simulated FIRE I stratocumulus cloud fields. The delta-Eddington method is a computationally cheap means to compute radiative transfer through a horizontally homogeneous cloud, whereas the Monte Carlo model utilizes the full three-dimensional structure of the cloud field. The delta-Eddington model was used to compute the plane-parallel cloud albedo $A_{PPH}$ from the horizontally slab-averaged value of the LWP. The optical depth $\tau$ of the cloud was calculated according to

$$\tau = \frac{3}{2}\frac{LWP}{\rho_l r_{eff}}, \tag{27}$$

with $\rho_l$ the density of liquid water and $r_{eff} = 10$ μm a constant cloud droplet effective radius. To focus on the effect of the cloud structure on the albedo, we used a fixed solar zenith angle of 53°. More details on the boundary conditions and the model parameters can be found in Duynkerke *et al.* (2004).

The effect of the horizontal inhomogeneities in the cloud LWP on the mean cloud albedo were assessed from the delta-Eddington model by computing the albedo for all $256 \times 256$ cloud columns in the LES domain. According to the ICA, the mean albedo of the horizontally inhomogeneous cloud ($A_{ICA}$) can then be obtained by horizontally averaging the albedos of all cloud subcolumns. The cloud inhomogeneity factor $\chi$ is determined by finding the optical depth $\tau_{eff}$ for which its plane-parallel albedo corresponds exactly to the mean albedo for a horizontally inhomogeneous cloud according to the ICA approach, $A(\tau_{eff}) = A_{ICA}$ such that

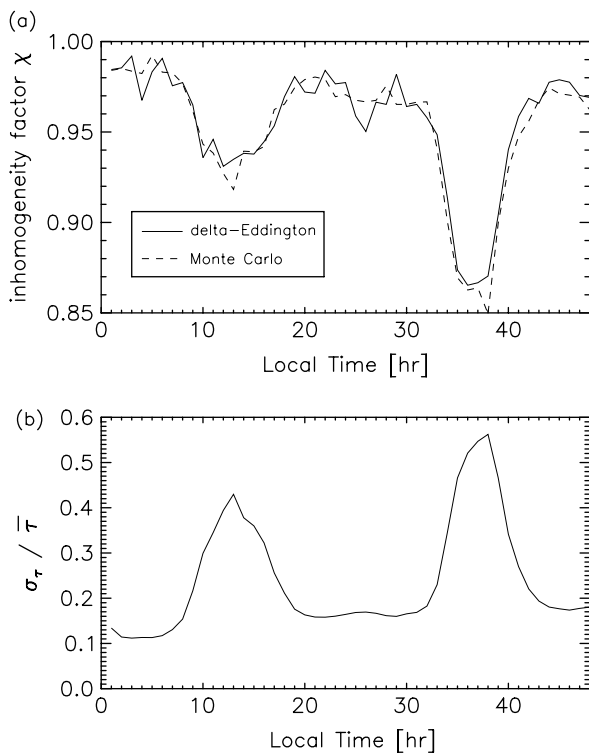$$\chi = \frac{\tau_{eff}}{\overline{\tau}}. \tag{28}$$

Figure 15. (a) The inhomogeneity factor, $\chi$, computed from instantaneous LES cloud fields. The solid line indicates results obtained from a delta-Eddington radiative transfer model, and the dotted line denotes results computed from I3RC Monte Carlo calculations. A fixed solar zenith angle, $\theta_0 = 53^0$, was used. (b) shows the standard deviation of the optical depth, $\sigma_\tau$, normalized by its mean value, $\overline{\tau}$.

Note that Rossow *et al.* (2002) define the inhomogeneity factor $\epsilon = 1 - \chi$. The mean cloud albedo ($A_{MC}$) was also computed using the full three-dimensional liquid water content fields as input for a Monte Carlo radiative transfer model. Note that this model uses the same model parameters as used for the delta-Eddington calculations.

Figure 15 shows that the differences in the inhomogeneity factor $\chi$ computed from the delta-Eddington and the Monte Carlo models are less than 0.02. This implies that under the present conditions the detailed three-dimensional spatial distribution of cloud liquid water appears to be of relatively little importance. Because a fixed solar zenith angle was used to compute the inhomogeneity factor, the temporal variations in $\chi$ can be explained only by variations in the mean and the variance of the optical depth. According to the Monte Carlo modelling results, the factor $\chi$ has a minimum value of about 0.85 during daytime when the ratio $\sigma_\tau/\overline{\tau}$ is maximum.

To explain these findings, Figure 16 displays contours of the inhomogeneity factor $\chi$ as a function of the mean optical depth $\overline{\tau}$ and its standard deviation normalized by the mean value, $\sigma_\tau/\overline{\tau}$. The inhomogeneity factor was computed with the delta-Eddington model where we systematically changed the width of an assumed Gaussian optical depth distribution. Note that for too large values of $\sigma_\tau$, negative values for the optical depth will arise, which can be interpreted as clear-air patches in the cloud layer. At this point the factor $\chi$ tends to decrease rapidly.
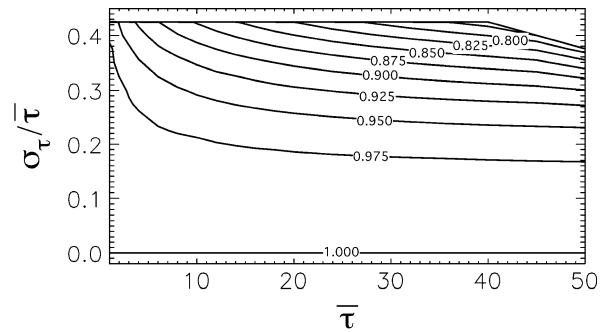


Figure 16. Contours of the inhomogeneity factor, $\chi$, as a function of the mean optical thickness, $\overline{\tau}$, and its normalized standard deviation, $\sigma_\tau/\overline{\tau}$. To compute the inhomogeneity factor $\chi$, a Gaussian distribution for $\tau$ was assumed.

The figure shows results only for cloud fractions larger than 0.99. For a given mean value of the optical depth, the inhomogeneity effect becomes increasingly important for larger optical depth variances. We conclude that solid clouds with $\overline{\tau} < 30$ and a Gaussian optical depth distribution will typically have an inhomogeneity factor $\chi > 0.8$.

According to Oreopoulos and Davies (1998), the albedo bias is dependent on the domain size of the cloud field. This is due to the fact that the variance of the LWP increases with increasing domain size (De Roode *et al.*, 2004). To investigate this effect from the LES cloud fields, we used the most inhomogeneous cloud field at $t = 36$ local time, and divided the LES horizontal domain into smaller subdomains, ranging from $2^2, 2^3, \ldots,$ to $2^7$ grid points. For these subdomains we computed the variance of the optical depth and the inhomogeneity factor $\chi$. To determine the latter, mean plane-parallel albedos were computed for every subdomain cloud field. Next, we averaged every set of equal subdomain size results. It is clear from Figure 17 that the total horizontal mean optical depth variance increases if the subdomain size becomes larger. Also, for subdomain sizes $< 10$ km, the albedo bias effect is insignificant as $\chi > 0.95$.

The inhomogeneity factors computed from the LES cloud fields are significantly larger than the value of about 0.7 found from microwave retrievals of LWP during FIRE I by Cahalan *et al.* (1994). This does not appear to be caused by an unrealistic simulated cloud structure, as the simulated LWP PDFs compare qualitively well to the FIRE I LWP analyses reported by Wood and Taylor (2001). In addition, the inhomogeneity values computed from the LES FIRE I cloud fields are in agreement with LES results of other stratocumulus cloud cases discussed by Bäuml *et al.* (2004). Oreopoulos and Cahalan (2005) studied satellite images of marine stratocumulus regimes, and observed values of $\chi$ greater than about 0.85 in July, consistent with the satellite values of Pincus *et al.* (1999) and Rossow *et al* (2002). As illustrated in Figure 16, $\chi$ values that do not deviate much from unity are typically associated with overcast grid points. This stresses the significant effect of the cloud fraction on the albedo bias
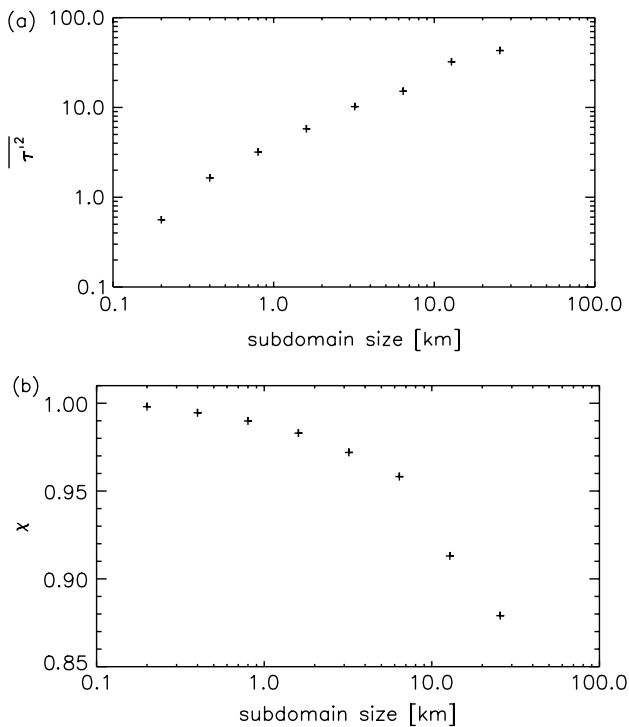
Figure 17. (a) The horizontal slab-mean variance of the optical depth and (b) the horizontal slab-mean inhomogeneity factor $\chi$, as a function of the subdomain size of the LES model. The mean values were computed by averaging over all subdomain results of the instantaneous cloud field at $t = 36$ hours local time.

(Barker *et al.*, 1996; Pincus *et al.*, 1999; Rossow *et al.*, 2002; Oreopoulos and Cahalan, 2005).

## 6.  Conclusions

Cloud fields obtained from a large-eddy simulation of the diurnal cycle of FIRE I stratocumulus are studied. It is found that the temperature and the total specific humidity fields in the cloud layer exhibit similar spatial structures to the liquid water path. The positive correlation between the total specific humidity and the temperature in the cloud layer indicates that relatively moist air is typically warmer and vice versa. Liquid water content fluctuations are found to be much smaller than the total specific humidity fluctuations, which is attributed to the temperature effect on the saturation specific humidity.

We present a model that takes into account the temperature effect on the saturation specific humidity. In this model we calculate liquid water fluctuations from the total specific humidity and a scale factor $\beta$. The $\beta$ factor gives a measure of the temperature effect on liquid water fluctuations. In the limit of vanishing temperature fluctuations, $\beta = 1$. However, if liquid water potential temperature fluctuations are negligibly small, it can be shown that $\beta$ should be much smaller. In particular, $\beta \approx 0.4$ for the FIRE I stratocumulus case. The reduced $\beta$ factor value may perhaps also be a better assumption for other stratocumulus cases. In particular, this will be the

case if positive liquid water potential temperature fluctuations caused by entrainment mixing of higher $\theta_l$ values from just above the inversion are strongly diminished by long-wave radiative cooling near the cloud top.

The LES results are used to develop a parametrization for LWP subcolumn fluctuations from total specific humidity fluctuations only. In a large-scale model, the latter can be computed from solving the prognostic equation for the total specific humidity variance (Tompkins, 2002). The presented model uses the $\beta$ factor and is capable of reproducing the actual LWP PDFs rather satisfactorily. Neglecting the effect of temperature fluctuations leads to LWP PDFs that are too broad.

The LES fields are also used to compute the difference between the albedo computed from the horizontal mean cloud LWP, and the albedo based on the actual horizontally inhomogeneous cloud field according to the Independent Column Approximation. This so-called albedo bias effect appears to be insignificant if the simulated clouds are optically thick, but becomes increasingly important for clouds that have a large ratio of the optical depth standard deviation to its mean value, $\sigma_\tau/\overline{\tau}$. This is typically the case for stratocumulus during daytime. The minimum value for the inhomogeneity factor $\chi$ as computed from the LES stratocumulus cloud fields is about 0.85.

With a delta-Eddington model, we calculated the inhomogeneity factor $\chi$ for a solid (unbroken) cloud layer with an assumed Gaussian optical depth distribution. We found a minimum value for $\chi$ of about 0.8. If the ratio of the optical depth standard deviation to its mean value decreases, the inhomogeneity factor becomes close to unity. Because the LWP variance tends to increase with increasing horizontal grid size, the inhomogeneity factor will therefore generally depend on the horizontal domain size of the large-scale model (Oreopoulos and Davies, 1998). Because of this strong dependence of the albedo bias on the optical depth variance, the application of a constant cloud inhomogeneity correction factor in a solar radiative transfer scheme seems rather crude. It calls for a more distinct approach like McICA that directly takes into account the subgrid variability of the LWP. From the delta-Eddington calculation for clouds with an assumed Gaussian optical depth distribution, we also noticed a sharp decrease in the inhomogeneity factor $\chi$ if clear-air columns are allowed in the cloud layer. This demonstrates that besides the detailed spatial liquid water distribution of the cloud, the cloud fraction is as important for an accurate computation of the solar radiative transfer.

The cloud albedo bias is principally due to fluctuations in the cloud optical depth. If in a GCM the variance $\overline{q_t'^2}$ is computed, it can be straightforwardly converted to the variance of the LWP. If we neglect the second term on the right-hand side of (26), $\overline{LWP'^2}$ may be approximated by

$$\overline{LWP'^2} = (\rho_0 \overline{H} \beta)^2 \, \overline{q_t'^2}. \qquad (29)$$

For a constant cloud droplet effective radius, using (27) the variance of the optical depth becomes

$$\overline{\tau'^2} = \left(\frac{3\rho_0 \overline{H} \beta}{2\rho_1 r_{\text{eff}}}\right)^2 \overline{q_t'^2}. \tag{30}$$

A more accurate estimation of $\overline{\tau'^2}$ can be made if one takes into account the variation of microphysical properties with height (Los and Duynkerke, 2000; Jeffery and Austin, 2003).

## Acknowledgements

## References

Barker HW, Räisänen P. 2004. Radiative sensitivities for cloud geometric properties that are unresolved by conventional GCMs. *Q. J. R. Meteorol. Soc.* **130**: 2069–2086.

Barker HW, Wielicki BA, Parker L. 1996. A parameterization for computing grid-averaged solar fluxes for inhomogeneous marine boundary layer clouds. Part II: Validation using satellite data. *J. Atmos. Sci.* **53**: 2304–2316.

Barker HW, Pincus R, Morcrette J-J. 2002. 'The Monte Carlo Independent Column Approximation: Application within large-scale models'. Proceedings from the GCSS Workshop. Kananaskis: Alberta, Canada.

Bäuml G, Chlond A, Roeckner E. 2004. Estimating the PPH-bias for simulations of convective and stratiform clouds. *Atmos. Res.* **72**: 317–328.

Cahalan RF, Ridgway W, Wiscombe WJ, Gollmer S, Harshvardhan. 1994. Independent pixel and Monte-Carlo estimates of stratocumulus albedo. *J. Atmos. Sci.* **51**: 3776–3790.

Cahalan RF, Oreopoulos L, Marshak A, Evans KF, Davis AB, Pincus R, Yetzer KH, Mayer B, Davies R, Ackerman TP, Barker HW, Clothiaux EE, Ellingson RG, Garay MJ, Kassianov E, Kinne S, Macke A, O'Hirok W, Partain PT, Prigarin SM, Rublev AN, Stephens GL, Szczap F, Takara EE, Várnai T, Wen G, Zhuravleva TB. 2005. The I3RC: Bringing together the most advanced radiative transfer tools for cloudy atmospheres. *Bull. Am. Meteorol. Soc.* **86**: 1275–1293.

Considine G, Curry JA, Wielicki B. 1997. Modeling cloud fraction and horizontal variability in marine boundary layer clouds. *J. Geophys. Res.* **102**: 13517–13525.

De Roode SR, Duynkerke PG, Jonker HJJ. 2004. Large-eddy simulation: How large is large enough? *J. Atmos. Sci.* **61**: 403–421.

Duynkerke PG, de Roode SR, van Zanten MC, Calvo J, Cuxart J, Cheinet S, Chlond A, Grenier H, Jonker PJ, Köhler M, Lenderink G, Lewellen D, Lappen C-L, Lock AP, Moeng C-H, Müller F,

Olmeda D, Piriou J-M, Sanchez E, Sednev I. 2004. Observations and numerical simulations of the diurnal cycle of the EUROCS stratocumulus case. *Q. J. R. Meteorol. Soc.* **130**: 3269–3296.

Harshvardhan, Randall DA. 1985. Comments on 'The parameterization of radiation for numerical weather prediction and climate models'. *Mon. Weather Rev.* **113**: 1832–1833.

Jeffery CA, Austin PH. 2003. Unified treatment of thermodynamic and optical variability in a simple model of unresolved low clouds. *J. Atmos. Sci.* **60**: 1621–1631.

Jonker HJJ, Duynkerke PG, Cuijpers JWM. 1999. Mesoscale fluctuations in scalars generated by boundary-layer convection. *J. Atmos. Sci.* **56**: 801–808.

Joseph JH, Wiscombe WJ, Weinman JA. 1976. The delta-Eddington approximation for radiative flux transfer. *J. Atmos. Sci.* **33**: 2452–2459.

Lilly D. 1968. Models of cloud-topped mixed layers under a strong inversion. *Q. J. R. Meteorol. Soc.* **94**: 292–309.

Los A, Duynkerke PG. 2000. Microphysical and radiative properties of inhomogeneous stratocumulus: Observations and model simulations. *Q. J. R. Meteorol. Soc.* **126**: 3287–3307.

Los A, Duynkerke PG. 2001. Parametrization of solar radiation in inhomogeneous stratocumulus: Albedo bias. *Q. J. R. Meteorol. Soc.* **127**: 1593–1614.

Moeng C-H. 2000. Entrainment rate, cloud fraction and liquid water path of PBL stratocumulus clouds. *J. Atmos. Sci.* **57**: 3627–3643.

Nicholls S. 1984. The dynamics of stratocumulus: Aircraft observations and comparisons with a mixed-layer model. *Q. J. R. Meteorol. Soc.* **110**: 783–820.

Oreopoulos L, Cahalan RF. 2005. Cloud inhomogeneity from MODIS. *J. Climate* **18**: 5110–5124.

Oreopoulos L, Davies R. 1998. Plane parallel albedo biases from satellite observations. Part I: Dependence on resolution and other factors. *J. Climate* **11**: 919–932.

Pincus R, McFarlane SA, Klein SA. 1999. Albedo bias and the horizontal variability of clouds in subtropical marine boundary layers: Observations from ship and satellites. *J. Geophys. Res.* **104**: 6183–6191.

Pincus R, Barker HW, Morcrette J-J. 2003. A fast, flexible, approximate technique for computing radiative transfer in inhomogeneous cloud fields. *J. Geophys. Res.* **108**: DOI: 10.1029/2002JD003322.

Räisänen P, Barker HW, Khairoutdinov MF, Li J, Randall D A. 2004. Stochastic generation of subgrid-scale cloudy columns for large-scale models. *Q. J. R. Meteorol. Soc.* **130**: 2047–2067.

Rossow WB, Delo C, Cairns B. 2002. Implications of the observed mesoscale variations of clouds for the Earth's radiation budget. *J. Climate* **15**: 557–585.

Stevens B. 2002. Entrainment in stratocumulus-topped mixed layers. *Q.J.R. Meteorol. Soc.* **128**: 2663–2690.

Tiedtke M. 1996. An extension of cloud-radiation parameterization in the ECMWF model: The representation of subgrid-scale variations of optical depth. *Mon. Weather Rev.* **124**: 745–750.

Tompkins AM. 2002. A prognostic parameterization for the subgrid-scale variability of water vapor and clouds in large-scale models and its use to diagnose cloud cover. *J. Atmos. Sci.* **59**: 1917–1942.

Wood R, Taylor JP. 2001. Liquid water path variability in unbroken marine stratocumulus cloud. *Q. J. R. Meteorol. Soc.* **127**: 2635–2662.

Wood R, Hartmann DL. 2006. Spatial variability of liquid water path in marine low cloud: The importance of mesoscale cellular convection. *J. Climate* **19**: 1748–1764.